Interdisciplinary Research in Medical Sciences Specialty
ISSN: 3062-4401
2026, Volume 6, Issue 1, Page No: 320-332

Available online at: www.galaxypub.co/page/journals

Galaxy Publication

Contribution of Metabolic, Perfusion, and Diffusion Imaging to the Improvement of Diagnosis and Outcome Prediction in H3K27-Altered Diffuse Midline Gliomas

Saif Al-Hinai[1]*, Amal Al-Balushi[1], Mohammed Al-Maskari[2], Sultan Al-Mahruqi[3]

[1]Department of Neuro-Oncology and Advanced Imaging, College of Medicine, Sultan Qaboos University, Muscat, Oman.
[2]Department of Metabolic and Perfusion Imaging, College of Medicine, University of Nizwa, Nizwa, Oman.
[3]Department of Diffuse Midline Glioma Research, College of Medicine, Dhofar University, Salalah, Oman.

***E-mail** ✉ saif.alhinai@squ.edu.om

Received: 10 May 2026; **Revised:** 26 June 2026; **Accepted:** 27 June 2026

ABSTRACT

The purpose of this investigation was to determine the added value of metabolic imaging, perfusion mapping, and diffusion kurtosis imaging (DKI) in accurately identifying and forecasting outcomes for patients with H3K27-altered diffuse midline gliomas (DMGs). A total of 95 individuals (mean age 16.98 years; 61.1% female) with brainstem masses were enrolled between June 2020 and May 2023. This cohort included 71 patients with H3K27-altered DMGs and 24 patients harboring H3K27 wild-type brainstem tumors (labeled non-DMGs). All participants underwent pre-operative conventional MRI along with advanced sequences: amide proton transfer-weighted (APTw) imaging, arterial spin labeling (ASL), and DKI. The study employed logistic regression and Cox proportional hazards models with leave-one-out cross-validation (LOOCV) to examine the standalone and synergistic contributions of these advanced MRI parameters for both diagnostic classification and survival prediction. Incorporating advanced MRI parameters markedly strengthened the ability to diagnose and prognosticate H3K27-altered DMGs. APTw imaging proved particularly useful, demonstrating significant associations with diagnosis (odds ratio [OR] = 3.81, p = 0.004) and overall survival (Hazard ratio [HR] = 1.89, p = 0.003). ASL-derived relative cerebral blood flow (rCBF) also enhanced diagnostic accuracy (OR = 7.74, p = 0.019) and prognostic stratification (HR = 2.87, p = 0.002). Meanwhile, DKI-derived mean diffusivity (MD) was strongly linked to the presence of H3K27-altered DMGs (OR = 0.03, p = 0.012). Multivariate analysis showed that APTw (OR = 3.41, p = 0.014) and MD (OR = 0.05, p = 0.049) functioned as independent diagnostic indicators, while APTw (HR = 1.66, p = 0.037) and rCBF (HR = 2.15, p = 0.038) emerged as independent predictors of overall survival (OS). The combination of metabolic, perfusion, and advanced diffusion imaging techniques provides substantial improvements in the identification and outcome prediction of H3K27-altered DMGs compared to traditional MRI features. These insights have the potential to guide more effective clinical management strategies.

Keywords: H3K27-altered diffuse midline gliomas, Amide proton transfer-weighted imaging (APTw), Arterial spin labeling (ASL), Diffusion kurtosis imaging (DKI), Diagnosis, Prognosis

How to Cite This Article: Al-Hinai S, Al-Balushi A, Al-Maskari M, Al-Mahruqi S. Contribution of Metabolic, Perfusion, and Diffusion Imaging to the Improvement of Diagnosis and Outcome Prediction in H3K27-Altered Diffuse Midline Gliomas. Interdiscip Res Med Sci Spec. 2026;6(1):320-32. https://doi.org/10.51847/bXK07IG9Ky

Introduction

H3K27-altered diffuse midline gliomas (DMGs) constitute highly malignant and incurable neoplasms within the central nervous system (CNS). As defined by the 2021 World Health Organization (WHO) classification of CNS tumors, they are assigned WHO Grade 4 status due to their infiltrative and rapidly progressive nature [1, 2]. These tumors are grouped under pediatric-type diffuse high-grade gliomas in the updated WHO framework [2]. While predominantly affecting children, they also occur in teenagers and adults [3]. DMGs represent about 80% of all brainstem tumors [4] and preferentially arise in midline CNS locations [5]. Most earlier research has contrasted

adult cases of DMGs against midline IDH-wildtype glioblastomas (GBMs) [6, 7]. In routine practice, however, clinicians must differentiate brainstem tumors from a wider spectrum of entities, such as various astrocytomas [8], pilocytic astrocytomas [9], and gangliogliomas [10], alongside GBMs. These lesions frequently display overlapping clinical symptoms and imaging appearances, making accurate separation challenging. Distinguishing H3K27-altered DMGs from H3K27 wild-type midline tumors (collectively termed non-DMGs) carries major implications for selecting appropriate therapies and estimating patient survival.

MRI remains the cornerstone non-invasive modality for detecting DMGs and evaluating therapeutic responses. Conventional MRI sequences, sometimes augmented by radiomic analysis or deep learning algorithms, have been explored for predicting H3K27 mutation status [11, 12] and survival outcomes [4, 13]. However, such approaches often yield features that are difficult to interpret in daily clinical decision-making. In addition, standard anatomical MRI does not adequately reflect the specific biological hallmarks associated with H3K27-altered DMGs.

In recent years, sophisticated MRI methods such as amide proton transfer-weighted (APTw) imaging, arterial spin labeling (ASL), and multi-shell diffusion acquisitions have emerged to probe tumor metabolism [14, 15], neovascularization [16, 17], and microstructural complexity [18-20]. Several recent publications have begun applying these tools to uncover pathological features of DMGs and assist in non-invasive diagnosis. Zhuo and colleagues [15] reported that APTw signal intensity, along with radiomic features extracted from APTw maps, exhibited robust capability in identifying H3K27 alterations, highlighting its potential as a novel imaging marker. Additional evidence suggests that H3K27-mutant DMGs tend to display increased cerebral blood flow (CBF), consistent with enhanced angiogenesis and aggressive behavior [21, 22]. Diffusion-weighted imaging (DWI) studies have also correlated lower apparent diffusion coefficient (ADC) measurements with greater tumor cellularity and inferior prognosis [23]. Nevertheless, standard DWI assumes Gaussian water diffusion and may overlook finer aspects of tissue architecture. Diffusion kurtosis imaging (DKI), which utilizes multi-shell diffusion data, better accounts for non-Gaussian diffusion properties, yielding more detailed information about cellular organization and the surrounding microenvironment [19]. One recent multi-shell diffusion MRI investigation demonstrated excellent separation between H3K27-altered and wild-type midline gliomas [24]. Despite these contributions, most existing studies have examined single imaging modalities in isolation and have not fully explored the combined power of metabolic, perfusion, and kurtosis imaging for characterizing H3K27-altered DMGs. Furthermore, no previous work has evaluated the prognostic utility of these advanced MRI techniques in this patient population—an area critical for treatment planning and follow-up.

To mirror actual clinical scenarios more faithfully, this study deliberately included a heterogeneous group of non-DMG midline tumors as the comparison cohort. The primary goals were to profile the metabolic, hemodynamic, and microstructural properties of H3K27-altered DMGs via APTw, ASL, and DKI, and to rigorously quantify the incremental benefit these parameters offer beyond conventional MRI for both diagnosis and survival prediction.

Materials and Methods

Study design

The overall study framework, detailing patient recruitment, imaging acquisition and analysis pipelines, parameter derivation, and statistical methodology, is summarized in **Figure 1**.

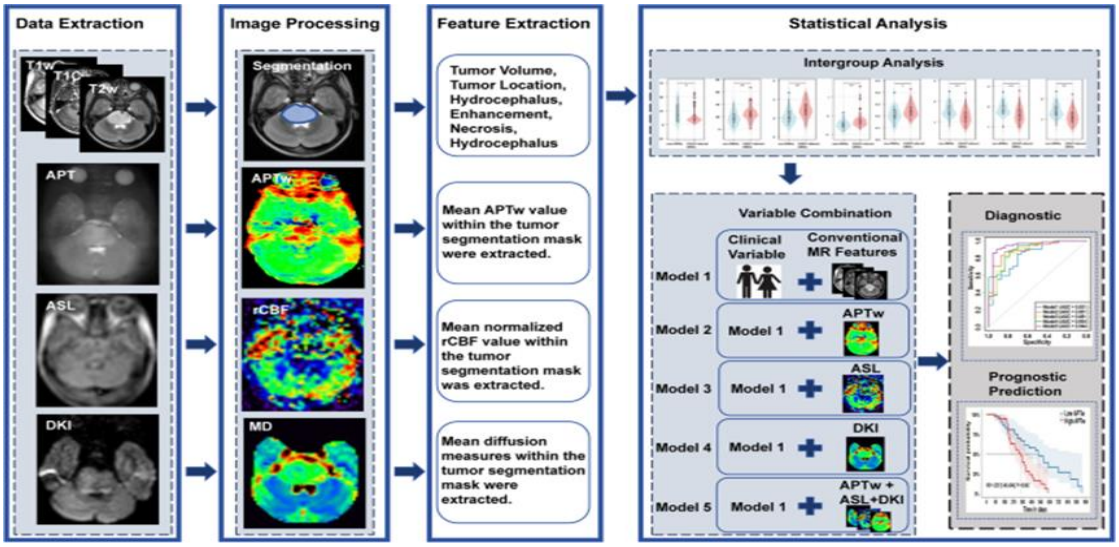

Figure 1. Overview of the Study. T1w: T1-weighted; T2w: T2-weighted; T1C: contrast-enhanced T1-weighted; APTw: amide proton transfer-weighted; ASL: arterial spin labeling; DKI: diffusion kurtosis imaging; rCBF: relative cerebral blood flow; MD: mean diffusivity

Participants

This prospective investigation recruited 125 patients with suspected brainstem tumors on clinical and radiological grounds from June 2020 through May 2023. Entry requirements included: (1) absence of any prior therapy; (2) availability of a complete preoperative MRI dataset; (3) confirmed brainstem location of the lesion on MRI; and (4) planned biopsy or resection leading to a definitive histopathological confirmation. Cases were ruled out for (1) unacceptable image quality or (2) lack of adequate pathology records.

Gathered clinical data covered patient age, sex, Karnofsky Performance Status (KPS) upon admission or consultation, and confirmed tumor type. Regular surveillance was conducted for every participant following diagnosis. Those lost to follow-up were censored on the date of their most recent recorded visit. Overall survival (OS) was calculated from the date of diagnosis until death from any etiology. Final data collection occurred on April 1, 2024, yielding a median follow-up period of 11.7 months (95% confidence interval [CI]: 3.7–28.8 months).

Pathological analysis

Tumor classification was conducted by a seasoned neuropathologist (X.L., 10 years of expertise) following the 2021 WHO classification of CNS tumors [2]. H3K27 alteration was identified through immunohistochemistry employing a mutation-specific antibody (Merck Millipore, Billerica, MA, USA). Assessment of the Ki-67 labeling index utilized immunohistochemistry with the MIB-1 (anti-Ki-67) antibody (Dako, Denmark). Neoplastic cells were distinguished using conventional morphological standards. Manual counting of total tumor cells and Ki-67-positive cells was performed in five selected hot spots at 400× magnification. The Ki-67 index was determined as the average proportion of positive cells from these sampled fields.

MRI acquisition

Imaging took place on a 3 T clinical MR scanner (Ingenia CX, Philips Healthcare, Best, The Netherlands) using a 32-channel head coil. The standard protocol comprised T1-weighted (T1w), T2-weighted (T2w), and contrast-enhanced T1-weighted (T1C) sequences.

APTw imaging employed a 3D fast spin-echo technique with these settings: repetition time (TR) = 5864 ms, echo time (TE) = 8.8 ms, flip angle (FA) = 90°, voxel dimensions = 2 mm × 2 mm × 6 mm, across 7 slices. Amide proton saturation was achieved with pulses at +3.5 ppm offset (relative to water) at a B1 amplitude of 2 μT lasting 2 seconds.

Normalization and interpolation of the Z-spectrum involved six extra volumes acquired at offsets of ±3.1 ppm, −3.5 ppm, ±3.9 ppm, and −1560 ppm. B0 field correction maps were generated from three additional +3.5 ppm

acquisitions with varied echo-time shifts using a Dixon approach to address inhomogeneity in the frequency domain [25]. SENSE acceleration factor = 1.6; total scan time = 1 min 54 s.

Pseudo-continuous arterial spin labeling (pCASL) was implemented for ASL with a 3D gradient and spin-echo readout. Key parameters were: 20 slices, 8 control/label pairs, TR/TE = 3903 ms/11 ms, SENSE factor = 1.3, labeling duration = 1800 ms, post-labeling delay (PLD) = 1500 ms, and acquisition time = 3 min 31 s.

Diffusion kurtosis imaging (DKI) utilized axial 2D spin-echo echo-planar imaging (SE-EPI) with parameters: TR/TE = 4000 ms/88 ms, FA = 90°, in-plane voxel size = 2.5 mm × 2.5 mm, acquisition matrix = 96 × 96, slice thickness = 2.5 mm, 60 slices, b-values = 0, 1000, 2000 s/mm² (48 diffusion-encoding directions for each non-zero b-value), SENSE factor = 2, multiband factor = 3, and scan duration = 6 min 48 s. Reverse phase-encoding B0 scans were obtained to enable distortion correction.

Tumor segmentation

Manual outlining of the solid tumor portion was performed on T2-weighted images, deliberately excluding areas of cyst formation, necrosis, or hemorrhage. Two neuroradiologists (M.W. and J.Q., each with over 5 and 10 years of neuroradiology experience, respectively) completed independent segmentations while blinded to H3K27 status. Anatomical guidance came from T1w and T1C images. The procedure used 3D Slicer software (version 4.10.2; www.slicer.org). A senior neuroradiologist (Y.D., 20 years of experience) subsequently reviewed and adjusted contours as needed. Inter-observer reliability for solid tumor delineation reached a Dice similarity coefficient of 0.89. The overlapping mask from both observers defined the final tumor region, and tumor volume was computed accordingly.

Image processing

APTw maps underwent automatic generation on the scanner console using its integrated pipeline. Voxel-level magnetization transfer ratio asymmetry (MTRasym) calculations isolated the amide proton transfer signal from confounding factors [26]. Corrections for B0 inhomogeneity were applied via dedicated field maps, and MTRasym at +3.5 ppm was derived and reported in percentage units. Co-registration of T2w images and tumor masks to APTw space allowed extraction of the average APTw value from the solid tumor compartment.

rCBF maps were derived from ASL datasets through the scanner's standard post-processing routine. Normalization to reduce inter-subject variability involved subtracting the mean gray-matter rCBF value and scaling by that mean. Gray-matter masks were generated from T1w images via Statistical Parametric Mapping (SPM12, https://www.fil.ion.ucl.ac.uk/spm/) and aligned to ASL data. Following co-registration of T2w images and tumor masks to ASL source images, the mean normalized rCBF within the tumor was recorded. This normalized metric is denoted simply as rCBF throughout subsequent evaluations.

Processing of DKI data relied on DIPY (https://dipy.org/), FMRIB Software Library (FSL) version 6.0 (https://fsl.fmrib.ox.ac.uk/fsl/fslwiki/FSL), and MRtrix3 (https://www.mrtrix.org/). Steps included denoising, distortion and eddy-current corrections, plus skull stripping. Derived metrics comprised fractional anisotropy (FA), mean diffusivity (MD), axial diffusivity (AD), radial diffusivity (RD), mean kurtosis (MK), axial kurtosis (AK), and radial kurtosis (RK). After aligning T2w images and tumor masks to the B0 volume, mean values for each metric were measured within the solid tumor.

Radiological evaluation

Conventional MRI features on T1w, T2w, and T1C sequences were independently rated by two neuroradiologists (M.W. and J.Q., with over 5 and 10 years of neuroradiology experience, respectively). Assessed features included: (1) tumor site (midbrain, pons, or medulla); (2) hydrocephalus presence; (3) contrast enhancement characteristics; and (4) necrosis. Hydrocephalus was defined by an Evans index greater than 0.3 on MRI [27]. Postoperative extent of resection (EOR) was graded as gross total resection (GTR: 100% EOR), subtotal resection (STR: >50% and <100% EOR), or partial resection (PR: <50% EOR). Disagreements were adjudicated by a senior neuroradiologist (Y.D., over 20 years of experience) for final consensus.

Statistical analysis

Analyses were carried out in R statistical software (version 4.2.3). Frequencies and percentages described categorical data, compared via Chi-square tests. Continuous measures underwent Student's t-test or Mann–Whitney U test as dictated by normality.

Diagnostic contributions of APTw, ASL, and DKI parameters were evaluated individually and jointly for differentiating H3K27-altered DMGs. Five multivariate logistic regression models incorporating leave-one-out cross-validation (LOOCV) were developed: Model 1 relied on clinical data and conventional MRI; Model 2 added APTw; Model 3 added ASL; Model 4 added DKI; and Model 5 integrated all three advanced techniques with baseline variables. Performance metrics (AUC, sensitivity, specificity, accuracy) were computed, with model comparisons performed using DeLong's test.

Prognostic contributions for overall survival in the H3K27-altered DMG subgroup were similarly assessed via five parallel multivariate Cox regression models with LOOCV. Model performance was gauged by concordance index (C-index). Supplementary evaluations involved Kaplan–Meier curves stratified according to imaging metrics, log-rank testing, and risk group stratification derived from the comprehensive Cox model (Model 5). A threshold of $p < 0.05$ indicated statistical significance.

Results and Discussion

Demographic, clinical, and conventional MRI characteristics

From 125 patients initially considered with brainstem gliomas, exclusions occurred due to: prior treatment (n=4), suboptimal APTw quality (n=6), inadequate ASL quality (n=5), poor DKI quality (n=10), and missing histology (n=5).

The analyzed cohort totaled 95 patients: 71 with confirmed H3K27-altered DMGs and 24 non-DMGs. Non-DMG pathologies included 7 pilocytic astrocytomas, 2 gangliogliomas, 7 wild-type GBMs, 6 astrocytomas (two Grade 4, one Grade 3, three Grade 2), one mixed glioneuronal tumor, and one gliosis. Illustrative examples of conventional MRI alongside quantitative parameter maps—APTw for metabolic activity, ASL-CBF for perfusion, and DKI-derived MD for diffusion—are presented for two representative cases in **Figure 2a**.

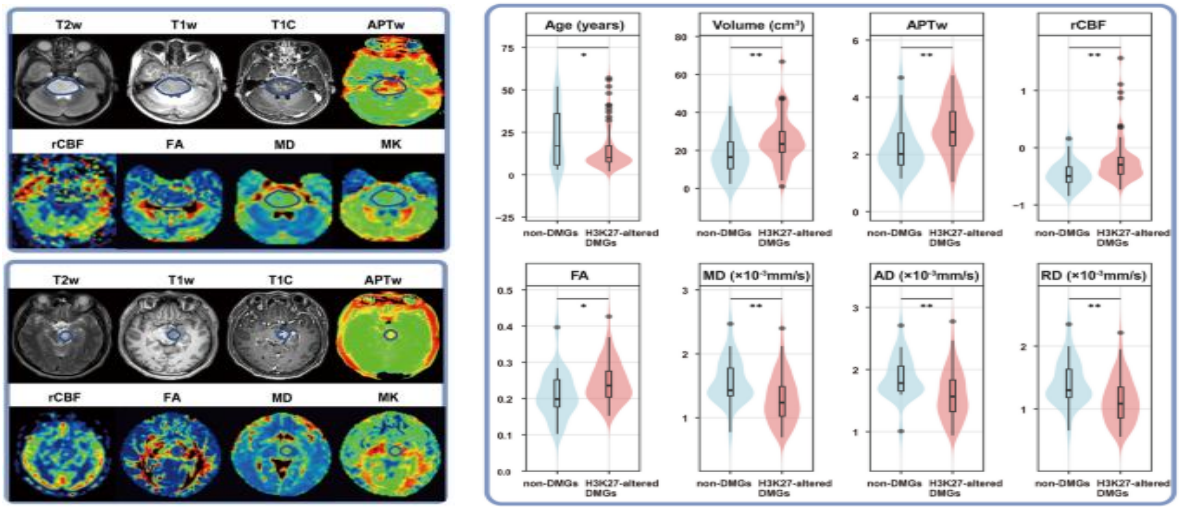

Figure 2. Panel A presents example standard MRI images together with metabolic, perfusion, and diffusion maps for cases involving H3K27-altered DMG compared to non-DMG tumors. a A 5-year-old girl diagnosed with H3K27-altered DMG; b A 42-year-old man with non-DMG (Grade 4 astrocytoma). Panel B outlines the key distinctions in clinical features and MRI parameters observed between the H3K27-altered DMG and non-DMG patient groups.

T1w: T1-weighted; T2w: T2-weighted; T1C: contrast-enhanced T1-weighted; APTw: amide proton transfer-weighted; rCBF: relative cerebral blood flow; FA: fractional anisotropy; MD: mean diffusivity; MK: mean kurtosis; AD: axial diffusivity; RD: radial diffusivity; * $p < 0.05$; ** $p < 0.01$; *** $p < 0.001$.Subjects with H3K27-altered DMGs tended to be substantially younger at diagnosis than those with non-DMGs (15.13 ± 1.58 years versus 22.46 ± 3.60 years, $p = 0.035$). Mean Karnofsky Performance Status (KPS) scores were notably reduced in the H3K27-altered DMG cohort relative to the non-DMG cohort (86.06 versus 97.08, $p = 0.012$). The overwhelming majority of H3K27-altered DMGs arose in the pons (66/71, 92.96 percent). In contrast, non-DMGs

were distributed across the pons (62.50 percent), medulla (8.33 percent), and midbrain (29.17 percent). Clear disparities emerged in the extent of resection (EOR) between groups: biopsy-only (40.85% vs. 16.67%), gross total resection (GTR: 16.90 percent vs. 62.50 percent), subtotal resection (STR: 9.86 percent vs. 16.67 percent), and partial resection (PR: 32.39 percent vs. 4.16 percent), all reaching statistical significance ($p < 0.001$) **(Table 1)**. Conventional MRI traits, including contrast enhancement, necrosis, and hydrocephalus, showed no meaningful differences between the H3K27-altered DMG and non-DMG groups **(Table 1)**.

Table 1. Demographics, clinical, and conventional MRI characteristics of patients with DMGs and non-DMGs

	All Patients (*N = 95*)	**non-DMGs (*N = 24*)**	***H3K27*-altered DMGs (*N = 71*)**	***p-value***
Age	16.98 ± 1.52	22.46 ± 3.60	15.13 ± 1.58	0.035*
Sex (%)				1.000
male	37 (38.95%)	9 (37.50%)	28 (39.44%)	
female	58 (61.05%)	15 (62.50%)	43 (60.56%)	
EOR (%)				< 0.001*
Biopsy	33 (34.74%)	4 (16.67%)	29 (40.85%)	
GTR	27 (28.42%)	15 (62.50%)	12 (16.90%)	
STR	11 (11.58%)	4 (16.67%)	7 (9.86%)	
PR	24 (25.26%)	1 (4.16%)	23 (32.39%)	
KPS	88.84 ± 1.81	97.08 ± 1.27	86.06 ± 2.30	0.012*
Location (%)				< 0.001*
Pons	81 (85.26%)	15 (62.50%)	66 (92.96%)	
Medulla	7 (7.37%)	2 (8.33%)	5 (7.04%)	
Midbrain	7 (7.37%)	7 (29.17%)	0 (0.00%)	
Enhancement (%)				1.000
No	35 (36.84%)	9 (37.50%)	26 (36.62%)	
Yes	60 (63.16%)	15 (62.50%)	45 (63.38%)	
Necrosis (%)				0.767
No	48 (50.53%)	11 (45.83%)	37 (52.11%)	
Yes	47 (49.47%)	13 (54.17%)	34 (47.89%)	
Hydrocephalus (%)				1.000
No	65 (68.42%)	16 (66.67%)	49 (69.01%)	
Yes	30 (31.58%)	8 (33.33%)	22 (30.99%)	
Volume (cm^3),median, (IQR)	22.7 (15.3,29.7)	16.4 (10.4,24.5)	23.4 (19.0,30.0)	0.008*
APTw,median, (IQR)	2.74 (2.07,3.45)	2.01 (1.63,2.74)	2.79 (2.30,3.50)	0.001*
rCBF,median, (IQR)	−0.35 (−0.50,−0.18)	−0.49 (−0.61,−0.34)	−0.30 (−0.46,−0.17)	0.002*
FA,median, (IQR)	0.23 (0.20,0.27)	0.20 (0.18,0.25)	0.24 (0.20,0.28)	0.015*
MD ($\times 10^{-3}$ mm/s),median, (IQR)	1.34 (1.09,1.60)	1.43 (1.34,1.78)	1.24 (1.02,1.49)	0.002*
AD ($\times 10^{-3}$ mm/s),median, (IQR)	1.65 (1.38,1.91)	1.78 (1.65,2.05)	1.57 (1.32,1.83)	0.002*
RD ($\times 10^{-3}$ mm/s),median, (IQR)	1.19 (0.96,1.44)	1.30 (1.18,1.63)	1.08 (0.86,1.35)	0.001*
MK,median, (IQR)	0.58 (0.51,0.68)	0.57 (0.46,0.72)	0.58 (0.52,0.67)	0.837
AK,median, (IQR)	0.57 (0.49,0.63)	0.54 (0.46,0.66)	0.57 (0.50,0.62)	0.461
RK,median, (IQR)	0.61 (0.54,0.75)	0.64 (0.47,0.80)	0.61 (0.55,0.73)	0.932

1. EOR= extent of resection; GTR= gross total resection; STR= subtotal resection; PR= partial resection; KPS= Karnofsky Performance Scale; APTw= amide proton transfer-weighted; rCBF= relative cerebral blood flow; FA= fractional anisotropy; MD= mean diffusivity; RD= radial diffusivity; AD= axial diffusivity; AK= axial kurtosis; MK= mean kurtosis; RK= radial kurtosis; HR= hazard ratio.
2. * denotes $p < 0.05$.

Metabolic, perfusion, and diffusion features in DMGs

When evaluating metabolic, perfusion, and diffusion parameters, individuals with H3K27-altered DMGs exhibited markedly distinct values from those with non-DMG tumors in the following measures: APTw (median 2.79 vs. 2.01), rCBF (median −0.30 vs. −0.49), FA (median 0.24 vs. 0.20), MD (median 1.24 vs. 1.43 × 10^{-3} mm/s), AD (median 1.57 vs. 1.78 × 10^{-3} mm/s), and RD (median 1.08 vs. 1.30 × 10^{-3} mm/s) (all $p < 0.05$). In contrast, the diffusional kurtosis imaging (DKI) parameters (MK, AK, and RK) revealed no statistically meaningful differences **(Table 1 and Figure 2b)**.

Metabolic, perfusion, and diffusion imaging enhances diagnostic accuracy for H3K27-altered DMGs

Five separate multivariate logistic regression models were developed based on variables found to be significant during univariate testing. Given the strong collinearity present among the various diffusion parameters, and because MD represents the average of AD and RD and thus acts as an overall indicator capturing both directional diffusion aspects [28], MD was chosen as the representative metric for the multivariable logistic regression and Cox regression analyses **(Table 2)**.

Table 2. Five multivariable regression models to distinguish *H3K27*-altered DMGs from non-DMGs

	Model 1		**Model 2**		**Model 3**		**Model 4**		**Model 5**	
	OR (95% CI)	***p***	***OR (95% CI)***	***p***	***OR (95% CI)***	***p***	***OR (95% CI)***	***p***	***OR (95% CI)***	***p***
Location										
Pons	ref		ref		ref		ref		ref	
Medulla	2.23(0.32,22.25)	0.447	2.19(0.24,26.99)	0.505	2.53(0.31,29.85)	0.414	1.53(0.17,20.00)	0.722	1.41(0.11,23.26)	0.798
Midbrain	NA		NA		NA		NA		NA	
Age	0.97(0.93,1.01)	0.183	0.98(0.94,1.03)	0.341	0.96(0.96,1.00)	0.079	0.95(0.90,0.99)	0.029*	0.95(0.89,1.00)	0.043*
KPS	0.91(0.81,0.98)	0.058	0.92(0.81,0.98)	0.064	0.92(0.81,0.99)	0.099	0.90(0.77,0.98)	0.066	0.94(0.82,1.01)	0.203
Volume	1.03(0.97,1.09)	0.411	1.02(0.96,1.08)	0.614	1.00(0.94,1.07)	0.991	1.05(0.99,1.14)	0.154	1.02(0.95,1.10)	0.578
APTw			3.81(1.65,10.65)	0.004*					3.41(1.39,10.28)	0.014*
rCBF					7.74(3.18,44.25)	0.019*			1.26(0.25,18.88)	0.265
MD							0.03(0.001,0.38)	0.012*	0.05(0.002,0.80)	0.049*
FA							0.88(0.16,4.57)	0.877	0.98(0.14,6.36)	0.982

1. *KPS* Karnofsky Performance Scale, *APTw* Amide proton transfer-weighted, *rCBF* Relative cerebral blood flow, *FA* Fractional anisotropy, *MD* Mean diffusivity, *OR* Odds ratios, *CI* Confidence interval, *ref* reference, *NA* Not available
2. *indicate $p < 0.0$

Model 1 included clinical variables and conventional MRI features; an AUC of Model 1 was 0.831**(Table 2 and Figure 3a)**.

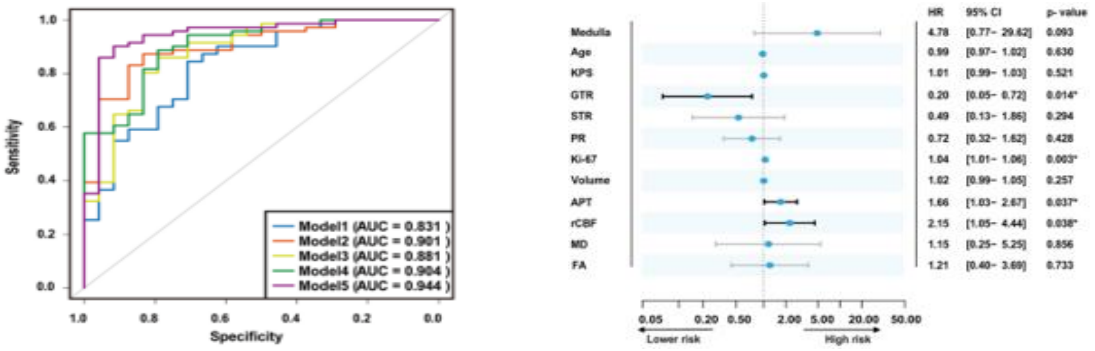

a) b)

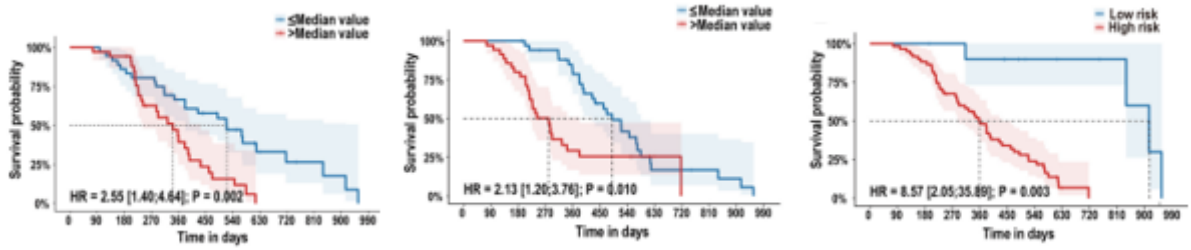

c) d) e)

Figure 3. A Receiver operating characteristic (ROC) curves showing the diagnostic ability of the five models to identify H3K27-altered DMGs. B Forest plot illustrating the prognostic Model 5. C Kaplan–Meier survival curves based on the median APTw value. D Kaplan–Meier survival curves based on the median rCBF value. E Kaplan–Meier survival curves comparing low- and high-risk patient groups.

ROC: receiver operating characteristic; KPS: Karnofsky Performance Scale; GTR: gross total resection; STR: subtotal resection; PR: partial resection; APTw: amide proton transfer-weighted; rCBF: relative cerebral blood flow; MD: mean diffusivity; FA: fractional anisotropy; HR: hazard ratio; CI: confidence interval. * $p < 0.05$.

Model performance details

When APTw was incorporated into Model 1 to create Model 2, APTw emerged as a strong independent factor with an odds ratio (OR) of 3.81 (95 percent CI: 1.65–10.65, p = 0.004). This resulted in an AUC of 0.901 for Model 2, representing a 0.07 increase compared to Model 1 (Delong's test p = 0.125).

In Model 3, which included rCBF alongside the variables in Model 1, rCBF showed an OR of 7.74 (95 percent CI: 3.18–44.25, p = 0.019), yielding an AUC of 0.881 — a 0.05 gain over Model 1 (Delong's test p = 0.216).

Model 4 combined DKI parameters (MD and FA) with Model 1 variables. Here, MD continued to function as an independent predictor (OR 0.03; 95% CI: 0.001–0.38, p = 0.012), producing an AUC of 0.904, which was 0.073 higher than Model 1 (Delong's test p = 0.046).

Model 5 integrated APTw, rCBF, MD, and FA into Model 1. Both APTw and MD stayed significant independent predictors, with ORs of 3.41 (95 percent CI: 1.39–10.28, p = 0.014) and 0.05 (95 percent CI: 0.002–0.80, p = 0.049), respectively. Model 5 reached the highest AUC of 0.994, improving by 0.163 over Model 1 (Delong's test p = 0.030).

Overall, Model 5, which combined clinical variables, conventional MRI findings, APTw, ASL, and DKI parameters, demonstrated the strongest diagnostic capability with the highest AUC among all tested models **(Figure 3a)**. Metabolic, perfusion, and diffusion imaging enhances prognostic assessment in H3K27-altered DMGs

For the 71 DMG patients who had overall survival (OS) information, five multivariate Cox proportional hazards regression models were developed following the same structure as the diagnostic models **(Table 3)**. Only variables that reached statistical significance ($p < 0.05$) in the univariate Cox regression analyses were carried forward into the multivariable models.

Table 3. Multivariable Cox regression models for predicting OS in *H3K27*-altered DMGs

	Model 1		**Model 2**		**Model 3**		**Model 4**		**Model 5**	
	HR (95% CI)	***p***	***HR (95% CI)***	***P***	***HR (95% CI)***	***p***	***HR (95% CI)***	***p***	***HR (95% CI)***	***p***
					Location					
Pons	ref		ref		ref		ref		ref	
Medulla	3.99(0.90, 17.60)	0.068	3.56(0.79, 16.0)	0.100	4.87(1.09, 21.81)	0.038	6.25(1.10, 35.70)	0.039	4.78(0.77, 29.6)	0.093
Age	1.00(0.98, 1.02)	0.876	1.00(0.97, 1.02)	0.737	1.00(0.97, 1.02)	0.805	1.00(0.97, 1.02)	0.788	0.99(0.97, 1.02)	0.630

KPS	1.00(0.98, 1.02)	0.802	1.00(0.99, 1.02)	0.619	1.01(0.99, 1.03)	0.583	1.00(0.98, 1.02)	0.932	1.01(0.99, 1.03)	0.521
					EOR					
Biopsy	ref		ref		ref		ref		ref	
GTR	0.28(0.08, 0.93)	0.038*	0.21(0.06, 0.71)	0.012*	0.27(0.08, 0.90)	0.033*	0.23(0.06, 0.81)	0.023*	0.20(0.05, 0.72)	0.014*
STR	0.52(0.15, 1.72)	0.286	0.45(0.13, 1.55)	0.230	0.51(0.15, 1.75)	0.332	0.64(0.18, 2.31)	0.482	0.49(0.13, 1.86)	0.294
PR	0.92(0.43, 1.97)	0.781	0.72(0.33, 1.59)	0.386	0.79(0.35, 1.77)	0.615	0.96(0.45, 2.06)	0.876	0.72(0.32, 1.62)	0.428
Ki-67	1.04(1.02, 1.06)	< 0.001*	1.03(1.01, 1.05)	0.015*	1.05(1.03, 1.07)	< 0.001*	1.04(1.02, 1.06)	< 0.001*	1.04(1.01, 1.06)	0.003*
Volume	1.03(1.00, 1.05)	0.082	1.02(0.99, 1.05)	0.185	1.02(0.99, 1.05)	0.173	1.02(0.99, 1.06)	0.110	1.02(0.99, 1.05)	0.257
APTw			1.89(1.24, 2.87)	0.003*					1.66(1.03, 2.67)	0.037*
rCBF					2.87(1.46, 5.65)	0.002*			2.15(1.05, 4.44)	0.038*
MD							1.69(0.45, 6.34)	0.382	1.15(0.25, 5.25)	0.856
FA							1.72(0.62, 4.80)	0.336	1.21(0.40, 3.69)	0.733

1. OS: overall survival; KPS: Karnofsky Performance Scale; EOR: extent of resection; GTR: gross total resection; STR: subtotal resection; PR: partial resection; APTw: amide proton transfer-weighted; rCBF: relative cerebral blood flow; FA: fractional anisotropy; MD: mean diffusivity; HR: hazard ratios; CI: confidence interval; ref: reference.
2. * indicates $p < 0.05$.

Prognostic modeling

Model 1 was based on clinical factors and standard MRI characteristics, yielding a C-index of 0.723.

In Model 2, APTw was added to Model 1 and remained an independent prognostic factor (HR 1.89; 95% CI: 1.24–2.87; p = 0.003). The C-index for Model 2 was 0.714, slightly lower than Model 1 by 0.009.

Model 3 incorporated rCBF into Model 1, where rCBF showed an HR of 2.87 (95% CI: 1.46–5.65, p = 0.002). This produced a C-index of 0.745, representing a 0.022 improvement over Model 1.

Model 4 included DKI parameters (MD and FA) along with Model 1 variables. MD had an HR of 1.69 (95% CI: 0.45–6.34, p = 0.382) and FA had an HR of 1.72 (95% CI: 0.62–4.80, p = 0.336). The C-index reached 0.729, a modest 0.006 gain over Model 1, though neither MD nor FA achieved statistical significance.

Model 5 combined APTw, rCBF, MD, and FA with the variables from Model 1. APTw continued as an independent predictor (HR 1.66; 95% CI: 1.03–2.67, p = 0.037), as did rCBF (HR 2.15; 95% CI: 1.05–4.44, p = 0.038). Model 5 attained a C-index of 0.742, higher than Model 1.

Ki-67 index and GTR proved to be significant prognostic factors across all models **(Table 3)**. The forest plot for Model 5 is displayed in **Figure 3b**. Patients were also divided according to median APTw and rCBF values, showing log-rank p-values of 0.002 and 0.010, with corresponding HRs of 2.55 and 2.13 **(Figures 3c and 3d)**. Risk scores derived from Model 5 separated patients into high-risk and low-risk categories, with the Kaplan–Meier analysis revealing an HR of 8.57 (p = 0.003) between these groups **(Figure 3e)**.

To investigate potential histological links underlying the imaging parameters that strengthened both diagnostic and prognostic models for H3K27-altered DMGs, correlations were examined between APTw, rCBF, MD, and the Ki-67 index. A significant association was observed between Ki-67 and APTw, while no such correlations existed for rCBF or MD.

This investigation employed metabolic, perfusion, and diffusion imaging techniques to evaluate their usefulness for diagnosis and survival prediction in H3K27-altered DMGs. The primary results can be summarized as follows: (1) Patients with H3K27-altered DMGs were notably younger, had reduced KPS scores, and displayed distinct APTw, rCBF, FA, MD, AD, and RD values relative to non-DMG cases. (2) APTw, rCBF, and MD each provided independent diagnostic value for identifying H3K27-altered DMGs, with their combination in Model 5 delivering

the best diagnostic accuracy (AUC 0.994, a 0.163 improvement over conventional MRI). (3) APTw and rCBF served as independent predictors of overall survival (OS) in H3K27-altered DMGs, and integrating them with MD and clinical variables produced the strongest prognostic model.

H3K27-altered DMGs represent a pediatric-type diffuse high-grade glioma category established in the 2021 WHO classification [2]. Our analysis confirmed that these patients were significantly younger than those with non-DMGs, consistent with tumor occurrence in the developing brain [29]. They also presented with lower KPS scores. Elevated APTw values are thought to indicate heightened tumor cell proliferation [30]. H3K27-altered DMGs displayed higher rCBF compared with non-DMGs, possibly linked to the relationship between rCBV and H3K27M-positive nuclear density [22]. These tumors additionally showed elevated FA and decreased diffusion values (MD, AD, RD). FA reflects diffusion anisotropy and greater microstructural complexity, whereas MD, AD, and RD measure water mobility, which is restricted in densely cellular tissues [20]. Collectively, these patterns point to increased tumor cell density and more intricate tissue architecture in H3K27-altered DMGs.

In the diagnostic models, APTw captures heterogeneous protein and peptide metabolism that may mirror glioma histopathology and molecular changes [14, 15, 30]. Higher APTw levels signal increased metabolic activity associated with active proliferation [30]. Incorporating APTw into models with clinical and conventional MRI data substantially boosted diagnostic accuracy for H3K27-altered DMGs. This is consistent with prior work by Zhuo *et al*. [15], who reported 86% accuracy using APTw radiomics for predicting H3K27 mutations in brainstem gliomas. Perfusion imaging also aided diagnosis, as rCBF demonstrated strong independent predictive power, aligning with Kathrani *et al*. [21], who linked rCBV ratios to histone mutation status. Diffusion metrics (MD, AD, RD) similarly contributed by reflecting higher cellular density [16], corroborating findings from Xu *et al*. [20] that densely packed cells restrict water diffusion. The integration of APTw, rCBF, and MD with clinical and conventional imaging achieved the top diagnostic performance (AUC 0.994), underscoring the complementary benefit of these advanced parameters.

For OS prediction in H3K27-altered DMGs, APTw independently forecasted survival, with higher values linked to poorer outcomes ($p = 0.002$), supporting observations by Joo *et al*. [30] in high-grade gliomas. This likely stems from associations with proliferation and invasiveness [31, 32]. We identified a notable correlation between APTw and Ki-67 index, where elevated Ki-67 indicates rapid cell division [33] and carries prognostic relevance in DMGs [34–36]. rCBF also proved to be an independent OS predictor, with higher values tied to shorter survival, consistent with Pang *et al*. [37] and the link between CBF, VEGF, and angiogenesis. Although diffusion metrics were useful diagnostically, they did not significantly influence OS prediction. The most effective prognostic model combined APTw, rCBF, MD, and clinical variables, capitalizing on their complementary roles, with APTw and rCBF as the key independent factors.

Overall, these findings highlight the utility of metabolic, perfusion, and diffusion imaging in both diagnosing and prognosticating H3K27-altered DMGs. However, several limitations should be noted. The study cohort comprised 95 patients (71 H3K27-altered DMGs and 24 non-DMGs), leading to class imbalance and a modest sample size. Although leave-one-out cross-validation (LOOCV) was applied for internal validation, it cannot completely overcome these issues. Larger multicenter studies are required for better generalizability. Second, incomplete treatment details beyond EOR limited adjustment for all potential confounders. Third, the median follow-up of 11.7 months may be too short for full long-term survival evaluation. Finally, the absence of histopathological or longitudinal imaging validation restricts direct linkage of imaging metrics to underlying tumor biology. Future research should address these gaps through expanded cohorts, comprehensive treatment data, extended follow-up, and integrated histological assessments.

Conclusion

This study demonstrated enhanced diagnostic precision and survival prediction for H3K27-altered DMGs through the integration of metabolic, perfusion, and diffusion metrics with conventional MRI and clinical information. The findings confirm that this multimodal approach offers substantial added value for accurate identification and prognostic evaluation of H3K27-altered DMGs.

Acknowledgments: None

Conflict of Interest: None

Financial Support: None

Ethics Statement: None

References

1. Louis DN, Perry A, Reifenberger G, von Deimling A, Figarella-Branger D, Cavenee WK, et al. The 2016 World Health Organization classification of tumors of the central nervous system: a summary. Acta Neuropathol. 2016;131(6):803–20.
2. Louis DN, Perry A, Wesseling P, Brat DJ, Cree IA, Figarella-Branger D, et al. The 2021 WHO classification of tumors of the central nervous system: a summary. Neuro Oncol. 2021;23(8):1231–51.
3. Hayashi N, Fukai J, Nakatogawa H, Kawaji H, Yoshioka E, Kodama Y, et al. Neuroradiological, genetic and clinical characteristics of histone H3 K27-mutant diffuse midline gliomas in the Kansai Molecular Diagnosis Network for CNS Tumors (Kansai Network): multicenter retrospective cohort. Acta Neuropathol Commun. 2024;12(1):120.
4. Leach JL, Roebker J, Schafer A, Baugh J, Chaney B, Fuller C, et al. MR imaging features of diffuse intrinsic pontine glioma and relationship to overall survival: report from the International DIPG Registry. Neuro Oncol. 2020;22(11):1647–57.
5. Lovibond S, Gewirtz AN, Pasquini L, Krebs S, Graham MS. The promise of metabolic imaging in diffuse midline glioma. Neoplasia. 2023;39:100896.
6. Raab P, Banan R, Akbarian A, Esmaeilzadeh M, Samii M, Samii A, et al. Differences in the MRI signature and ADC values of diffuse midline gliomas with H3 K27M mutation compared to midline glioblastomas. Cancers (Basel). 2022;14(6):1432.
7. Sim Y, Choi SH, Lee N, Park YW, Ahn SS, Chang JH, et al. Clinical, qualitative imaging biomarkers, and tumor oxygenation imaging biomarkers for differentiation of midline-located IDH wild-type glioblastomas and H3 K27-altered diffuse midline gliomas in adults. Eur J Radiol. 2024;173:111384.
8. Chen LH, Pan C, Diplas BH, Xu C, Hansen LJ, Wu Y, et al. The integrated genomic and epigenomic landscape of brainstem glioma. Nat Commun. 2020;11(1):3077.
9. Pan C, Li T, Zhang M, Wang Y, Xiao X, Zhang P, et al. A novel radiological classification of midbrain pilocytic astrocytomas and its implication for surgical management: a single-institution experience of 57 cases. J Neurosurg. 2024;140(6):1527–39.
10. Acharya S, Liu JF, Tatevossian RG, Chiang J, Qaddoumi I, Gajjar A, et al. Risk stratification in pediatric low-grade glioma and glioneuronal tumor treated with radiation therapy: an integrated clinicopathologic and molecular analysis. Neuro Oncol. 2020;22(8):1203–13.
11. Chauhan RS, Kulanthaivelu K, Kathrani N, Kotwal A, Bhat MD, Saini J, et al. Prediction of H3K27M mutation status of diffuse midline gliomas using MRI features. J Neuroimaging. 2021;31(6):1201–10.
12. Pan CC, Liu J, Tang J, Chen X, Chen F, Wu YL, et al. A machine learning-based prediction model of H3K27M mutations in brainstem gliomas using conventional MRI and clinical features. Radiother Oncol. 2019;130:172–9.
13. Liu X, Jiang Z, Roth HR, Anwar SM, Bonner ER, Mahtabfar A, et al. Early prognostication of overall survival for pediatric diffuse midline gliomas using MRI radiomics and machine learning: a two-center study. Neuro-Oncol Adv. 2024;6(1):vdae108.
14. von Knebel DN, Kroh F, Breitling J, Konig L, Maksimovic S, Grass S, et al. CEST imaging of the APT and ssMT predict the overall survival of patients with glioma at the first follow-up after completion of radiotherapy at 3T. Radiother Oncol. 2023;184:109694.
15. Zhuo Z, Qu L, Zhang P, Duan Y, Cheng D, Xu X, et al. Prediction of H3K27M-mutant brainstem glioma by amide proton transfer-weighted imaging and its derived radiomics. Eur J Nucl Med Mol Imaging. 2021;48(13):4426–36.
16. Hou H, Chen W, Diao Y, Wang Y, Zhang L, Wang L, et al. 3D amide proton transfer-weighted imaging for grading glioma and correlating IDH mutation status: added value to 3D pseudocontinuous arterial spin labelling perfusion. Mol Imaging Biol. 2023;25(2):343–52.

17. Qiu J, Wu K, Zhu M, Chen CY, Luo Y, Liu Y, et al. Using quantitative MRI to study the association of isocitrate dehydrogenase (IDH) status with oxygen metabolism and cellular structure changes in glioma. Eur J Radiol. 2022;155:110502.
18. Figini M, Riva M, Graham M, Castelli GM, Fernandes B, Grimaldi M, et al. Prediction of isocitrate dehydrogenase genotype in brain gliomas with MRI: single-shell versus multishell diffusion models. Radiology. 2018;289(3):788–96.
19. Zhao J, Wang YL, Li XB, Hu MS, Li ZH, Song YK, et al. Comparative analysis of the diffusion kurtosis imaging and diffusion tensor imaging in grading gliomas, predicting tumour cell proliferation and IDH-1 gene mutation status. J Neurooncol. 2019;141(1):195–203.
20. Xu X, Zhang P, Zhuo Z, Duan Y, Qu L, Cheng D, et al. Prediction of H3K27M alteration status in brainstem glioma using multi-shell diffusion MRI metrics. J Magn Reson Imaging. 2023;58(1):203–14.
21. Kathrani N, Chauhan RS, Kotwal A, Kulanthaivelu K, Bhat MD, Saini J, et al. Diffusion and perfusion imaging biomarkers of H3 K27M mutation status in diffuse midline gliomas. Neuroradiology. 2022;64(8):1519–28.
22. Calmon R, Dangouloff-Ros V, Varlet P, Deroulers C, Philippe C, Debily MA, et al. Radiogenomics of diffuse intrinsic pontine gliomas (DIPGs): correlation of histological and biological characteristics with multimodal MRI features. Eur Radiol. 2021;31(12):8913–24.
23. Leibetseder A, Leitner J, Mair MJ, Meckel S, Hainfellner JA, Aichholzer M, et al. Prognostic factors in adult brainstem glioma: a tertiary care center analysis and review of the literature. J Neurol. 2022;269(3):1574–83.
24. Zhang H, Liu K, Ba R, Zhang Z, Zhang Y, Chen Y, et al. Histological and molecular classifications of pediatric glioma with time-dependent diffusion MRI-based microstructural mapping. Neuro Oncol. 2023;25(6):1146–56.
25. Togao O, Keupp J, Hiwatashi A, Yamashita K, Kikuchi K, Yoneyama M, et al. Amide proton transfer imaging of brain tumors using a self-corrected 3D fast spin-echo Dixon method: comparison with separate B(0) correction. Magn Reson Med. 2017;77(6):2272–9.
26. Zhou J, Heo HY, Knutsson L, van Zijl PCM, Jiang S. APT-weighted MRI: techniques, current neuro applications, and challenging issues. J Magn Reson Imaging. 2019;50(2):347–64.
27. Toma AK, Holl E, Kitchen ND, Watkins LD. Evans' index revisited: the need for an alternative in normal pressure hydrocephalus. Neurosurgery. 2011;68(4):939–44.
28. Arab A, Wojna-Pelczar A, Khairnar A, Szabo N, Ruda-Kucerova J. Principles of diffusion kurtosis imaging and its role in early diagnosis of neurodegenerative disorders. Brain Res Bull. 2018;139:91–8.
29. Liu I, Jiang L, Samuelsson ER, Marco Salas S, Beck A, Hack OA, et al. The landscape of tumor cell states and spatial organization in H3–K27M mutant diffuse midline glioma across age and location. Nat Genet. 2022;54(12):1881–94.
30. Joo B, Han K, Ahn SS, Choi YS, Chang JH, Kang SG, et al. Amide proton transfer imaging might predict survival and IDH mutation status in high-grade glioma. Eur Radiol. 2019;29(12):6643–52.
31. Park JE, Kim HS, Park KJ, Kim SJ, Kim JH, Smith SA. Pre- and posttreatment glioma: comparison of amide proton transfer imaging with MR spectroscopy for biomarkers of tumor proliferation. Radiology. 2016;278(2):514–23.
32. Regnery S, Adeberg S, Dreher C, Oberhollenzer J, Meissner JE, Goerke S, et al. Chemical exchange saturation transfer MRI serves as predictor of early progression in glioblastoma patients. Oncotarget. 2018;9(47):28772–83.
33. Uxa S, Castillo-Binder P, Kohler R, Stangner K, Muller GA, Engeland K. Ki-67 gene expression. Cell Death Differ. 2021;28(12):3357–70.
34. Zheng L, Gong J, Yu T, Zou Y, Zhang M, Nie L, et al. Diffuse midline gliomas with histone H3 K27M mutation in adults and children: a retrospective series of 164 cases. Am J Surg Pathol. 2022;46(6):863–71.
35. Jiang H, Yang K, Ren X, Cui Y, Li M, Lei Y, et al. Diffuse midline glioma with H3 K27M mutation: a comparison integrating the clinical, radiological, and molecular features between adult and pediatric patients. Neuro Oncol. 2020;22(5):e1–9.
36. Maeda S, Ohka F, Okuno Y, Aoki K, Motomura K, Takeuchi K, et al. H3F3A mutant allele specific imbalance in an aggressive subtype of diffuse midline glioma, H3 K27M-mutant. Acta Neuropathol Commun. 2020;8(1):8.

37. Pang H, Dang X, Ren Y, Zhuang D, Qiu T, Chen H, et al. 3D-ASL perfusion correlates with VEGF expression and overall survival in glioma patients: comparison of quantitative perfusion and pathology on accurate spatial location-matched basis. J Magn Reson Imaging. 2019;50(1):209–20.